



**HAL**  
open science

## **Reconstructing Ocean Surface Current Combining Altimetry and Future Spaceborne Doppler Data**

Clement Ubelmann, Gérald Dibarboure, Lucile Gaultier, Aurélien Ponte, Fabrice Arduin, Maxime Ballarotta, Yannice Faugère

### ► **To cite this version:**

Clement Ubelmann, Gérald Dibarboure, Lucile Gaultier, Aurélien Ponte, Fabrice Arduin, et al.. Reconstructing Ocean Surface Current Combining Altimetry and Future Spaceborne Doppler Data. *Journal of Geophysical Research. Oceans*, 2021, 126 (3), <10.1029/2020JC016560>. <insu-03439173>

**HAL Id: insu-03439173**

**<https://insu.hal.science/insu-03439173v1>**

Submitted on 22 Nov 2021

**HAL** is a multi-disciplinary open access archive for the deposit and dissemination of scientific research documents, whether they are published or not. The documents may come from teaching and research institutions in France or abroad, or from public or private research centers.

L'archive ouverte pluridisciplinaire **HAL**, est destinée au dépôt et à la diffusion de documents scientifiques de niveau recherche, publiés ou non, émanant des établissements d'enseignement et de recherche français ou étrangers, des laboratoires publics ou privés.



HAL Authorization

# Reconstructing Ocean Surface Current Combining Altimetry and Future Spaceborne Doppler Data

Clement Ubelmann<sup>1</sup>, Gérald Dibarboure<sup>2</sup>, Lucile Gaultier<sup>3</sup>, Aurélien Ponte<sup>4</sup>,  
Fabrice Ardhuin<sup>4</sup>, Maxime Ballarotta<sup>5</sup> and Yannice Faugère<sup>5</sup>

<sup>1</sup>Ocean Next, La Terrasse, France

<sup>2</sup>Centre National d'Etudes Spatiales, Toulouse, France

<sup>3</sup>Ocean Data Lab, Plouzané, France

<sup>4</sup>Ifremer, Plouzané, France

<sup>5</sup>Collecte Localisation Satellite, Ramonville Saint Agne, France

## Key Points:

- The Near Inertial Oscillations (NIOs) challenge the mapping of total surface current from future Spaceborne Doppler data and Altimetry.
- The challenge can be tackled with inversion schemes accounting for the coherency of NIOs, allowing inversion of the current components.
- Altimetry is an essential component to disentangle geostrophy from the other components of the total surface current.

**Abstract**

Two methods for the mapping of ocean surface currents from satellite measurements of sea level and future current vectors are presented and contrasted. Both methods rely on the linear and Gaussian analysis framework with different levels of covariance definitions. The first method separately maps sea level and currents with single-scale covariance functions and leads to estimates of the geostrophic and ageostrophic circulations. The second maps both measurements simultaneously and projects the circulation onto 4 contributions: geostrophic, ageostrophic rotary, ageostrophic divergent and inertial. When compared to the first method, the second mapping moderately improves the resolution of geostrophic currents but significantly improves estimates of the ageostrophic circulation, in particular near-inertial oscillations. This method offers promising perspectives for reconstructions of the ocean surface circulation. Even the hourly dynamics can be reconstructed from measurements made locally every few days because nearby measurements are coherent enough to help fill the gaps. Based on numerical simulation of ocean surface currents, the proposed SKIM mission that combines a nadir altimeter and a Doppler scatterometer with a 300 km wide swath (with a mean revisit time of 3 days) would allow the reconstruction of 50% of the near-inertial variance around an 18 hour period of oscillation.

**Plain Language Summary**

Ocean surface currents are caused by a variety of phenomena that varies at different space and time scales. Here we mainly consider the two dominant contributions. The first is the current resulting from the quasi-equilibrium between the sloping sea level and the Coriolis force, slowly evolving over a few days. The second is also associated with the Coriolis force, but out of equilibrium: oscillating currents caused by rapid changes of the wind with a narrow range of periods around a natural period of oscillation that increase with latitude from 12 hours at the poles. For many applications it is desirable to separate these two contributions, for example to compute transports associated to the slowly evolving component and to evaluate the amount of kinetic energy pumped by the wind, mostly in the fast oscillations. This separation is easy with hourly sampled in situ measurements, but few are available. Here we show that we can perform this separation using satellite passes with measurements of sea level and a swath of surface current vectors, as can be measured by proposed future satellites. The fast oscillations can be reproduced even if data is available every few days, thanks to their spatial patterns and temporal coherence.

**1 Introduction**

The ocean surface current, a key variable for many scientific and operational applications, is only partially and indirectly observed from space. Altimetry provides the geostrophic component of the current (Fu et al., 1988), which is a dominant contribution to surface transport in most of the oceans, effectively resolving wavelengths larger than about 200 km wavelength (Ballarotta et al., 2019). The ageostrophic component, not synoptically observed yet, is locally sampled from drifting buoys (Elipot et al., 2016) or High Frequency Radars near the coasts (Kim et al., 2008) and is typically dominated by near-inertial oscillations that are an important source of energy for ocean mixing (Yu et al., 2019). If model estimates for ageostrophic current are available, in particular for the low-frequency part (Rio et al., 2014) the uncertainties are still high. Filling this gap with satellite measurements of the total surface current is the topic of active research, with several emerging concepts of spaceborne Doppler radar for either 1 km resolution local studies such as SEASTAR (Gommenginger et al., 2019) or global mapping at 10 to 30 km resolution with SKIM (Arduin, Brandt, et al., 2019, using a 300 km wide swath), STREAM (a new proposal for ESA Earth Explorer 11, using a 900 km wide swath) or

67 WaCM (Rodríguez et al., 2019, using a 1200 to 1800 km wide swath), see Arduin, Chapron,  
 68 et al. (2019) for a review. Similarly to HF radar, these latter would provide radial com-  
 69 ponents for multiple azimuth angles, from which the two-dimensional current vector could  
 70 be assessed.

71 As for any satellite observation of a geophysical variable evolving in time and space,  
 72 an important question is the ability to map the field given the instrument spatial res-  
 73 olution and time revisits. Satellite altimetry offers a very interesting example. Altime-  
 74 ters measure the anomaly of the Sea Surface Height (SSH) that contains the signature  
 75 of various processes in the ocean spanning over a wide range of scales, some at a much  
 76 higher frequency than the typical 10-day revisits of the Jason satellite orbits for instance.  
 77 In practice, barotropic tides and response to high frequency winds and pressure turned  
 78 out to be well handled (Carrère and Lyard (2003), Gille and Hughes (2001)) either from  
 79 independent or empirical models, allowing accurate reconstructions of the mesoscale eddy  
 80 field and , when combined with the mean dynamic topography, derived geostrophic cur-  
 81 rents (Le Traon & Dibarboure, 2002) with limited aliasing contamination. The case of  
 82 total surface current brings new challenges. One of them is related to the signature of  
 83 Near Inertial Oscillations (NIOs) (D’Asaro, 1985) which translates a natural mode of res-  
 84 onance in the ocean that is excited by winds at the surface. NIOs surface current have  
 85 average root mean square (RMS) magnitudes of 7-15 cm/s at mid and high latitudes (Elipot  
 86 et al., 2010; Yu et al., 2019), often comparable to the magnitude of currents in mesoscale  
 87 eddies. In spite of efforts to understand and model NIOs (Pollard and Millard (1970),  
 88 D’Asaro (1985), Whitt and Thomas (2015)), the predictability of NIOs, especially in phase,  
 89 is not yet accurate (for instance, a few hours offset in the wind reanalysis would disturb  
 90 the phase leading to wrong predictions). Interactions with mesoscale also affect NIO prop-  
 91 agation and dispersion which complicates its modeling (Young & Jelloul, 1997).

92 Relying on independent models of the high-frequency surface current is therefore  
 93 not yet guaranteed. Although Doppler radar concepts may allow shorter time revisits  
 94 than altimetry thanks to relatively wide swaths (Rodriguez et al., 2018), they may not  
 95 directly sample inertial periods, e.g. a 18 hours period at 40° of latitude requires a re-  
 96 visit time of 9 hours for which a swath wider than 2500 km is necessary, which does not  
 97 appear feasible with a single satellite mission. Therefore the reconstruction of surface  
 98 current in time and space from space-borne Doppler is a challenge.

99 The focus of this paper is to explore this reconstruction challenge in simulation,  
 100 taking the practical example of the SKIM Doppler concept combined with altimetry, us-  
 101 ing basic and improved mapping methods accounting for the physical properties of NIOs.  
 102 The skills of the reconstruction will be evaluated quantitatively for both geostrophic and  
 103 ageostrophic components in the North Atlantic basin.

## 104 2 Reconstruction methods

### 105 2.1 Background on linear analysis

106 The different mapping approaches explored in this study are all derived from the  
 107 linear and Gaussian mapping framework reviewed below . We assume a state to estimate,  
 108 noted  $\mathbf{x}$ , and partial observations, noted  $\mathbf{y}$ , that can be related to the state with a lin-  
 109 ear operator  $\mathbf{H}$  such as:

$$\mathbf{y} = \mathbf{H}\mathbf{x} + \epsilon \quad (1)$$

110 where  $\epsilon$  is an independent signal (e.g. observation error) not related to the state. If we  
 111 define  $\mathbf{B}$  the covariance matrix of  $\mathbf{x}$  and  $\mathbf{R}$  the covariance matrix of  $\epsilon$ , both variables be-  
 112 ing assumed Gaussian, then the linear estimate writes

$$\mathbf{x}^a = \mathbf{B}\mathbf{H}^T(\mathbf{H}\mathbf{B}\mathbf{H}^T + \mathbf{R})^{-1}\mathbf{y}. \quad (2)$$

113 This formulation, known as Optimal Interpolation, requires the inversion of a matrix of  
 114 the same size as the observation vector  $\mathbf{y}$ . When the number of observations exceeds the  
 115 size of the state to resolve, it can be interesting to use an equivalent formulation given  
 116 by the Sherman-Morrison-Woodbury transformation, allowing an inversion in state space,  
 117 with a matrix of the size of the state vector  $\mathbf{x}$ ,

$$\mathbf{x}^a = (\mathbf{H}^T \mathbf{R}^{-1} \mathbf{H} + \mathbf{B}^{-1})^{-1} \mathbf{H}^T \mathbf{R}^{-1} \mathbf{y}. \quad (3)$$

118 This second formulation is particularly useful when considering transformed states ex-  
 119 pressed in orthogonal bases (see section 2.3.1 where  $\mathbf{B}$  becomes diagonal and the whole  
 120 system gets easier to invert). If we note  $\mathbf{K}$  the linear operator such as  $\mathbf{x}^a = \mathbf{K}\mathbf{y}$  from eq.  
 121 (2) or eq.(3), the covariance matrix of analysis error is given by

$$\mathbf{B}^a = (\mathbf{I} - \mathbf{K}\mathbf{H})\mathbf{B} \quad (4)$$

122 This latter can be used to characterize the uncertainty of the solution.

## 123 2.2 Basic mappings

124 In the basic mapping approaches, we perform separate mappings of the SSH and  
 125 total surface current involving simple covariance functions in the  $\mathbf{B}$  matrix defined sep-  
 126 arately for each variable. Then the geostrophic component is given by the derivation of  
 127 SSH maps and the ageostrophic component by subtraction of the geostrophic compo-  
 128 nent to the total current.

### 129 2.2.1 For SSH: the standard Aviso/CMEMS mapping

130 To map the SSH, we first map the Sea Level Anomaly (SLA), defined in reference  
 131 to the long-term mean. We followed, as in the standard Aviso/CMEMS mapping, a basic  
 132 formulation derived from Eq.2. The observation vector  $\mathbf{y}$  is the SLA observations,  
 133 noted  $\mathbf{h}^o$ . The state vector  $\mathbf{x}$  is the gridded SLA. The observation operator  $\mathbf{H}$  (a tri-linear  
 134 interpolator transforming the gridded state SLA to equivalent along-track SLA) is not  
 135 written explicitly: in practice, the matrices  $\mathbf{B}\mathbf{H}^T$  and  $\mathbf{H}\mathbf{B}\mathbf{H}^T$ , representing the covari-  
 136 ance of the signal in the (grid,obs) and (obs, obs) spaces, are directly written with the  
 137 analogical formula of the covariance model as described in (Pujol et al., 2016). The  $\mathbf{R}$   
 138 matrix, for representativity and instrumental errors, is assumed diagonal. Since the co-  
 139 variance of SLA is assumed to vanish beyond a few hundreds of kilometers in space and  
 140 beyond 10 to 20 days in time ((Le Traon & Dibarboure, 2002)), separate inversions are  
 141 performed locally selecting observations over time and space windows adjusted to these  
 142 values. In practice, the number of observations being limited to less than 1000, the in-  
 143 version in observation space is computationally manageable. Details on the map produc-  
 144 tion are given in (Pujol et al., 2016). From the SLA maps, the SSH maps are given with  
 145 the addition of the long-term mean subtracted before the mapping.

### 146 2.2.2 For total surface current: a bi-variate weighted least square

147 The total surface current has different covariance structures than SSH, and does  
 148 not benefit from the long history of developments with operational systems (at least when  
 149 the measurements are scattered in space and azimuth angles as in the SKIM concept).  
 150 As a first level processing, we therefore choose a basic filter, where eq.(3) is applied lo-  
 151 cally to solve for a single current vector  $\mathbf{x} = [u, v]^T$  from the radial velocity observa-  
 152 tions nearby within a time-space radius. In this context,  $\mathbf{B}$  can be considered as infinite,  
 153 and eq. (3) reduces to the following bivariate least square formula

$$[u, v]^T = (\mathbf{H}^T \mathbf{R}^{-1} \mathbf{H})^{-1} \mathbf{H}^T \mathbf{R}^{-1} \mathbf{u}_r^o, \quad (5)$$

154 where  $\mathbf{u}_r^o$  are the radial velocity observations. The  $\mathbf{R}$  matrix represents the covariances  
 155 of  $\mathbf{u}_r^o$  errors, namely the representativity error and Doppler measurement error, both as-  
 156 sumed diagonal. Note that  $\mathbf{R}^{-1}$  can also be called the weight matrix  $\mathbf{W}$ , the weights  
 157 being the inverse of observation error variances (set to  $0.2^2 \text{ (m/s)}^2$  for the problem con-  
 158 sidered in section 3, which is an optimal value also including representativity errors). These  
 159 weights also take into account the time and space radius, set to 40 km and 10 days in  
 160 section 3, with a Hamming window. Finally, the observation operator  $\mathbf{H}$  can be writ-  
 161 ten from the vector of  $\mathbf{u}_r^o$  azimuth angles  $\theta_1 \dots \theta_p$  as follows ,

$$\mathbf{H} = \begin{bmatrix} \cos(\theta_1) & \sin(\theta_1) \\ \vdots & \vdots \\ \cos(\theta_p) & \sin(\theta_p) \end{bmatrix} \quad (6)$$

162 where  $p$  is the size of the observation vector. Since  $\mathbf{B}$  tends to infinity, the covariances  
 163 of analysis error  $\mathbf{B}^a$  given by the limit of eq. (4) are written as

$$\mathbf{B}^a = \mathbf{H}^T \mathbf{R}^{-1} \mathbf{H}. \quad (7)$$

164 A geometrical illustration of the solution is shown in Figure 1, with the ellipses of the  
 solution uncertainty given by the  $\mathbf{B}^a$  matrix of size  $(2 \times 2)$ . Note that at least two ob-

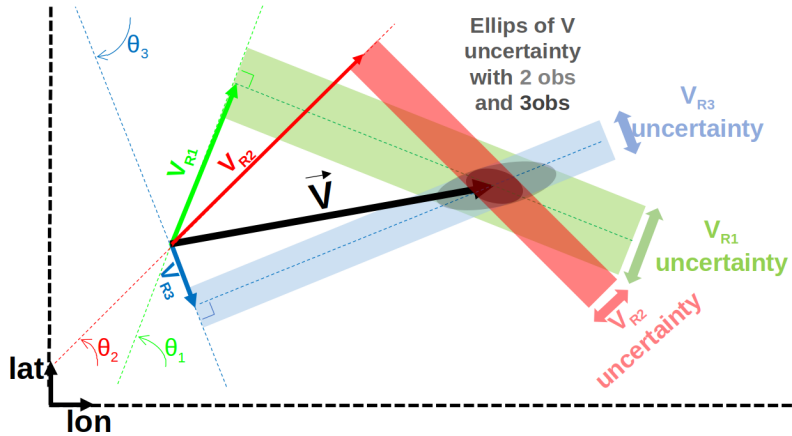


Figure 1: Scheme of the basic surface current mapping algorithm based on a bi-variate weighted least square, from at least two radial Doppler observations at different azimuth  $\theta$  (here there are 3 observations  $V_{R1}$ ,  $V_{R2}$ ,  $V_{R3}$  ).

165 servations at different  $\theta$  angles are necessary to ensure invertibility of eq.(5), which is also  
 166 illustrated on Figure 1. This is why the time-space radius must be carefully set with re-  
 167 spect to the observation sampling.  
 168

### 169 2.2.3 Geostrophic and ageostrophic current gridded maps

170 The geostrophic current ( $\mathbf{u}_g, \mathbf{v}_g$ ) is directly derived from the mapped SSH,

$$\begin{cases} u_g = -\frac{g}{f_c} \frac{\partial SSH}{\partial y} \\ v_g = \frac{g}{f_c} \frac{\partial SSH}{\partial x} \end{cases} \quad (8)$$

171 where  $f_c$  is the Coriolis frequency, which is a function of latitude. The ageostrophic es-  
 172 timates ( $\mathbf{u}_{ag}, \mathbf{v}_{ag}$ ) are obtained by subtraction to the total surface current ( $\mathbf{u}, \mathbf{v}$ ) of 2.2.2,

$$\begin{cases} u_{ag} = u - u_g \\ v_{ag} = v - v_g \end{cases} \quad (9)$$

173 These geostrophic and ageostrophic current estimates will be considered as the basic map-  
 174 ping solutions in section 4.

### 175 2.3 Improved mapping

176 The improved mapping also relies on linear analysis framework but with extended  
 177 state, extended observation vector and multivariate covariances. For practical reasons,  
 178 the inversion problem is framed in a reduced sub-component space such as to accommo-  
 179 date the number of observations in large spatio-temporal windows. This is particularly  
 180 interesting to handle multiple signals of various scales in time and/or space.

#### 181 2.3.1 Formulation

We consider an extended state vector  $\mathbf{x}$  composed by  $N$  physical components (e.g.  
 geostrophy, low and high frequency ageostrophy as proposed in section 2.3.2)

$$\mathbf{x} = (\mathbf{x}_1^T, \dots, \mathbf{x}_N^T)^T. \quad (10)$$

182 Each component  $\mathbf{x}_k$  contains the surface topography and surface current variables to be  
 183 resolved in the grid space, noted  $\mathbf{x}_k = (\mathbf{h}_k^T, \mathbf{u}_k^T, \mathbf{v}_k^T)^T$ . The key aspect of the method is  
 184 a rank reduction of the state vector, through a sub-component decomposition, such as  
 185  $\mathbf{x}_k$  can be written as

$$x_k = \begin{bmatrix} \Gamma_{k,h} \\ \Gamma_{k,u} \\ \Gamma_{k,v} \end{bmatrix} \eta_k = \Gamma_k \eta_k \quad (11)$$

186 where  $\eta_k$  is the reduced state vector for component  $k$ ,  $\Gamma_{k,h}$ ,  $\Gamma_{k,u}$ , and  $\Gamma_{k,v}$  are the sub-  
 187 component matrices in topography and currents. Note that for some components, one  
 188 of the block can be set to zeros (e.g. if ageostrophy component is considered with zero  
 189 contribution on SSH). Their concatenation is called  $\Gamma_k$  which is the matrix transform-  
 190 ing the reduced state vector in the grid space for topography and currents. In practice,  
 191  $\Gamma_k$  will be a wavelet decomposition of the time-space domain, with elements of appro-  
 192 priate temporal and spatial scales to represent the component  $k$ . These wavelet scales,  
 193 and their specified variance set with a diagonal matrix noted  $\mathbf{Q}_k$ , will define the equiv-  
 194 alent covariance model  $\mathbf{B}_k$  in the grid space for component  $k$

$$\mathbf{B}_k = \Gamma_k \mathbf{Q}_k \Gamma_k^T \quad (12)$$

195 The observation vector  $\mathbf{y}$  is also extended to the observed surface topography and sur-  
 196 face current noted  $\mathbf{y} = (\mathbf{h}^o{}^T, \mathbf{u}_r^o{}^T)^T$ . Then, if  $\mathbf{H}_k$  is the observation operator for com-  
 197 ponent  $k$  (from grid space to observation space), we note  $\mathbf{G}_k = \mathbf{H}_k \Gamma_k$  the sub-component  
 198 matrix expressed in observation space. In these conditions, the observation vector  $\mathbf{y}$  is  
 199 the sum of all component contributions plus the unexplained signal  $\epsilon$  (instrument error  
 200 and representativity),

$$\mathbf{y} = \sum_{k=1}^N \mathbf{G}_k \eta_k + \epsilon \quad (13)$$

201 If we use the notation  $\eta = (\eta_1^T, \dots, \eta_N^T)^T$  for the concatenation of the sub-component state  
 202 vectors, and  $\mathbf{G} = (\mathbf{G}_1, \dots, \mathbf{G}_N)$ , then we have,

$$\mathbf{y} = \mathbf{G}\eta + \epsilon \quad (14)$$

203 Applying the same transformation from eq. (1) to eq. (3), to the reduced state vector  
 204  $\eta$ , the global solution is written

$$\eta^{\mathbf{a}} = (\mathbf{G}^T \mathbf{R}^{-1} \mathbf{G} + \mathbf{Q}^{-1})^{-1} \mathbf{G}^T \mathbf{R}^{-1} \mathbf{y} \quad (15)$$

205 where  $\mathbf{Q}$  is the covariance matrix of  $\eta$ , expressed as the concatenation of the diagonal  
 206 matrices  $\mathbf{Q}_k$  for each component. Finally the solution in the reduced-space projects into  
 207 the grid space with the following relation,

$$\mathbf{x}^{\mathbf{a}} = \mathbf{\Gamma} \eta^{\mathbf{a}} \quad (16)$$

208 In practice, in order to solve for eq. (15), each block of  $\mathbf{G}$  is directly filled from the  
 209 analytical expression of the reduced-space elements (wavelets in section 2.3.2) constitut-  
 210 ing the columns of the matrix. Also, in many situations, the  $(\mathbf{G}^T \mathbf{R}^{-1} \mathbf{G} + \mathbf{Q}^{-1})$  matrix,  
 211 noted  $\mathbf{A}$  hereafter, would be too large to be inverted (and even written) explicitly. We  
 212 use a pre-conditioned conjugate gradient method to solve for  $\eta = \mathbf{A}^{-1} \mathbf{z}$  where  $\mathbf{z} = \mathbf{G}^T \mathbf{R}^{-1} \mathbf{y}$   
 213 is a vector of reduced-state size computed initially from  $\mathbf{G}$  and the observation vector  
 214  $\mathbf{y}$ . The algorithm involves many iterations of  $\mathbf{A}\eta$  computations for updated  $\eta$ . Note that  
 215 when  $\mathbf{A}$  is too large to be written explicitly, the result  $\mathbf{A}\eta$  can still be computed in two  
 216 steps from a matrix multiplication of  $\mathbf{G}$  then of  $\mathbf{G}^T$ . Once the convergence for the so-  
 217 lution  $\eta$  is reached, the projection in physical grid space given by Eq. (16) is applied se-  
 218 quentially, by summing the analytical expression of the wavelets applied to grid coordi-  
 219 nates (the columns of  $\mathbf{\Gamma}$ ), separately for each component  $k$ .

220 As in any inversion based on linear analysis, the result strongly relies on the choice  
 221 of covariance models, here defined by the reduced elements of each component. The choices  
 222 of these elements are discussed in the following section.

### 223 **2.3.2 Application to simultaneous mapping of geostrophy, low and high** 224 **frequency ageostrophy**

225 We propose to apply the above formulation for four components ( $N = 4$ ), con-  
 226 sidering that the surface current is dominated by geostrophy, low frequency ageostro-  
 227 phy (splitting the low-frequency flow in rotationnal and divergent components for prac-  
 228 tical reasons) and high frequency ageostrophy, for which specific wavelet bases will be  
 229 defined.

#### 230 **2.3.2.1 Geostrophy**

231 Geostrophy is the component that has a signature on both topography and currents,  
 232 where to expect some synergy between the altimetry and doppler observations. We de-  
 233 fine here the gridded variable  $\mathbf{H}_1$  to resolve, and the corresponding gridded geostrophic  
 234 current field  $(\mathbf{U}_1, \mathbf{V}_1)$  writes

$$\begin{cases} U_1 = -\frac{g}{f_c} \frac{\partial H_1}{\partial y} \\ V_1 = \frac{g}{f_c} \frac{\partial H_1}{\partial x} \end{cases} \quad (17)$$

235 The proposed reduced state for geostrophy is based on an element decomposition of  $\mathbf{H}_1$ ,  
 236 expressed by  $\mathbf{\Gamma}_{1,h}$  with wavelets of various wavelength and temporal extensions. This  
 237 will allow to approximate the standard covariance models used in altimetry mapping,  
 238 accounting for specific variations with wavelength and time. A given  $p$  element of the  
 239 decomposition  $\mathbf{\Gamma}_{1,h}$  is expressed as follows

$$\mathbf{\Gamma}_{1,h}[i, p] = \cos(k_{x,p}(x_i - x_p) + k_{y,p}(y_i - y_p) + \Phi_p) * f_{\text{tap}}\left(\frac{x_i - x_p}{L_{x_p}}, \frac{y_i - y_p}{L_{y_p}}, \frac{t_i - t_p}{L_{t_p}}\right) \quad (18)$$

240 where  $i$  is a given grid index of coordinates  $(x_i, y_i, t_i)$ . For the ensemble of  $p$ ,  $\Phi_p$  is al-  
 241 ternatively 0 and  $\pi/2$ , such as all subcomponents are defined by pairs of sine and cosine  
 242 functions to allow the phase degree of freedom.  $[CU]k_{x,p}$  and  $k_{y,p}$  are zonal and merid-  
 243 ional wavenumbers respectively, set to vary in the mappable mesoscale range (between  
 244 80km to 800km for the problem considered in section 3, with a spacing inversely propor-  
 245 tional to the wavelet extensions, allowing to represent a signal of any intermediate wave-  
 246 length).  $(x_p, y_p, t_p)$  are the coordinates of a space-time pavement. The function  $f_{\text{tap}}$  lo-  
 247 calizes the sub-component in time and space (at scales  $L_{t_p}$ ,  $L_{x_p}$  and  $L_{y_p}$  respectively)  
 248 as geostrophy has local extension of covariances. It is expressed as

$$f_{\text{tap}}(\delta x, \delta y, \delta t) = \begin{cases} \cos(\pi\delta x/2) \times \cos(\pi\delta y/2) \times \cos(\pi\delta t/2), & \text{for } (|\delta x|, |\delta y|, |\delta t|) < (1, 1, 1) \\ 0, & \text{elsewhere} \end{cases} \quad (19)$$

249 In practice, for the problem considered in section 3,  $L_{x_p}$  and  $L_{y_p}$  will be set to 1.5 the  
 250 wavelength of element  $p$  and  $L_{t_p}$  to the decorrelation time scale of Aviso maps, on the  
 251 order of 10 days in this region. Then, the same element  $p$  of the decomposition has also  
 252 an expression in geostrophic current (through the geostrophic relation Eq.17) written  
 253 in the  $\Gamma_{1,u}$  and  $\Gamma_{1,v}$  matrices

$$\begin{cases} \Gamma_{1,u}[i, p] = -g (\partial\Gamma_{1,h}[i, p]/\partial y_i) / f_c, \\ \Gamma_{1,v}[i, p] = g (\partial\Gamma_{1,h}[i, p]/\partial x_i) / f_c. \end{cases} \quad (20)$$

254 As an illustration,  $\Gamma_{1,h}[:, p]$  is shown on Figure 2 upper left panel, in plain color and  
 255  $\Gamma_{1,u}[:, p]$ ,  $\Gamma_{1,v}[:, p]$  in arrows. Here, this  $p^{\text{th}}$  component has a dominant wavelength  $\lambda =$   
 256  $\frac{2\pi}{\sqrt{k_{x,p}^2 + k_{y,p}^2}}$  in a given direction. The lower-left panel represents the temporal extension  
 257 of the sub-component set by  $L_{t_p}$ . The whole time-space domain is paved with similar  
 258 sub-components, along coordinates  $(x_p, y_p, t_p)$  for wavelengths between 80km and 800km  
 259 spanning in all directions of the plane. The ensemble can be seen as a wavelet basis. Fi-  
 260 nally, each sub-component  $p$  is assigned an expected variance in the  $\mathbf{Q}_1$  matrix, consis-  
 261 tent with the power spectrum observed from altimetry at the corresponding wavelength  
 262 with isotropy assumption.

263 For a given point  $i$  on the time-space grid (312°E, 40°N, day 10), the representor  
 264  $\Gamma_{1,h}[\mathbf{i}, :] \mathbf{Q} \Gamma_{1,h}$  is plotted on Figure 3, shown as a function of space (left panel) and as  
 265 a function of time (right panel). It illustrates the equivalent covariance function, which  
 266 is quite similar to what is currently used for altimetry mapping with OI inverted in ob-  
 267 servation space.

268 As mentioned in section 2.3.1, the inversion involves the construction of  $\mathbf{G}_1$  ma-  
 269 trix (see Eq.13), whose  $p^{\text{th}}$  column is represented on the right panel of Figure 2 consid-  
 270 ering altimetry tracks and scattered radial velocity observations at various azimuth an-  
 271 gles described later in section 3. Here, the arrows are the projection of the  $(\Gamma_{1,u}[:, p], \Gamma_{1,v}[:, p])$   
 272 along the various instrument azimuth angles and the colored dots the bilinear in-  
 273 terpolation at nadir altimetry coordinates.

### 2.3.2.2 Low-frequency ageostrophy: rotational part

274 The low-frequency ageostrophy cannot be reduced a priori, as for geostrophy, to  
 275 a single potential scalar field. However, if working with the zonal and meridional cur-  
 276 rent  $\mathbf{U}$  and  $\mathbf{V}$  would be a first option to build the reduced state, we decided to work with  
 277 the rotational and divergent current functions as they are scalars fields more likely to  
 278 have isotropic features than the directional variables  $\mathbf{U}$  and  $\mathbf{V}$ . Assuming isotropy of the  
 279 scalar fields practically allows easier reduced space decomposition. This paragraph deals  
 280 with the rotational flow, defined by a gridded variable  $\mathbf{P}$  (potential) to resolve, such as  
 281

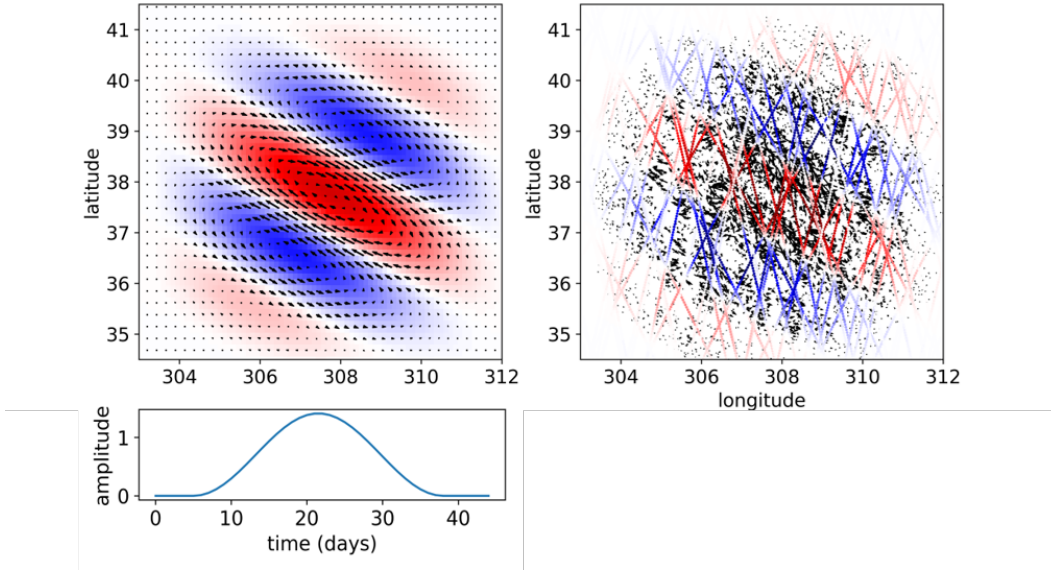


Figure 2: Illustration of a sub-component belonging to the mesoscale geostrophic component. The upper-left panel represents its expression in the grid space (= a column of the  $\Gamma_1$  matrix), in color for the topography ( $\Gamma_{1,h}$ ) and arrows for the current ( $\Gamma_{1,u}$  and  $\Gamma_{1,v}$ ), as a function of space. The lower-left panel represent the temporal modulation. The right panel represents the same sub-component in observation space considering altimetry tracks and scattered radial velocity observations at various azimuth angles, noted  $\mathbf{G}_1$  declined in  $\mathbf{G}_{1,h}$  (colors) and  $\mathbf{G}_{1,u_r}$  (arrows).

282 the gridded SSH and surface current ( $\mathbf{H}_2, \mathbf{U}_2, \mathbf{V}_2$ ) for this component are written

$$\begin{cases} H_2 = 0 \\ U_2 = -\frac{\partial P}{\partial y} \\ V_2 = \frac{\partial P}{\partial x} \end{cases} \quad (21)$$

283  $\mathbf{H}_2 = \mathbf{0}$  since we consider no contributions of  $\mathbf{P}$  on SSH. A reduced state is considered  
 284 for  $\mathbf{P}$ , constructed with single time/space window elements allowing the representation  
 285 of the field down to a certain regularity in time and space. The proposed decomposition  
 286 is much simpler than for topography, because the scales involved are larger in space and  
 287 we did not find the necessity to tune the covariance model beyond to get acceptable re-  
 288 sults. The reduced state is represented in the time-space domain by the following  $\Gamma_{2,P}$   
 289 matrix

$$\Gamma_{2,P}[i, p] = f_{\text{tap}}\left(\frac{x_i - x_p}{L_x}, \frac{y_i - y_p}{L_y}, \frac{t_i - t_p}{L_t}\right) \quad (22)$$

290 where  $f_{\text{tap}}$  is defined by Eq. 19. Here again,  $(x_p, y_p, t_p)$  are the coordinates to a space  
 291 and time pavement. In practice,  $L_x, L_y$  and  $L_t$  correspond to the decorrelation scales  
 292 (in time and space) of the reduced space. Using Eq 21, the matrices  $\Gamma_{2,h}$ ,  $\Gamma_{2,u}$  and  $\Gamma_{2,v}$   
 293 writes

$$\begin{cases} \Gamma_{2,h}[i, p] = 0 \\ \Gamma_{2,u}[i, p] = -\frac{\partial \Gamma_{2,P}[i, p]}{\partial y_i} \\ \Gamma_{2,v}[i, p] = \frac{\partial \Gamma_{2,P}[i, p]}{\partial x_i} \end{cases} \quad (23)$$

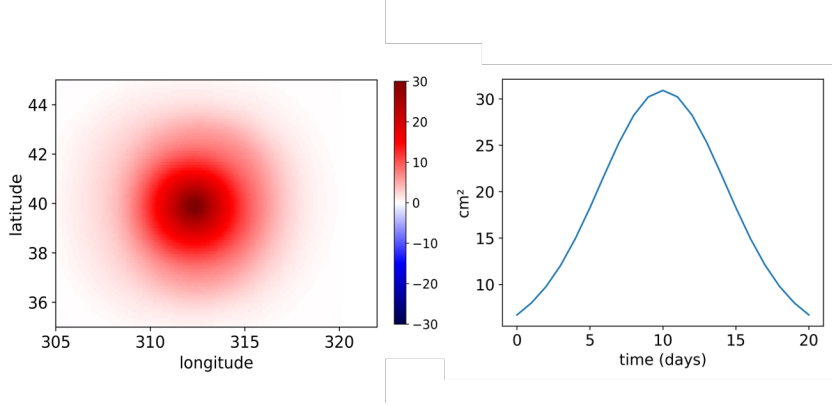


Figure 3: Illustration of the representor  $\mathbf{\Gamma}_{1_h}[i, :] \mathbf{Q} \mathbf{\Gamma}_{1_h}$  for a given point  $i$  on the time-space grid (312°E, 40°N, 10 days) represented as a function of space at 10 days (left panel) and as a function of time at 312°E, 40°N.

294 As an illustration, the  $p^{\text{th}}$  column of  $(\mathbf{\Gamma}_{2_u}, \mathbf{\Gamma}_{2_v})$  is represented on Figure 4. Here again,  
 295 the whole time-space domain is paved with similar wavelet sub-components along co-  
 296 ordinates  $\mathbf{x}_p$ ,  $\mathbf{y}_p$  and  $\mathbf{t}_p$ . The equivalent covariance model obtained from Eq.12, not shown,  
 297 is overall similar to what is shown on Fig.2 for geostrophy, with a more basic spatial func-  
 298 tion only driven by  $L_x$  and  $L_y$ . It is set larger in space and shorter in time, aiming to  
 299 capture large and more rapid signals than geostrophy. Targeting shorter scales in space  
 300 would not be compatible with the observation dataset considered. In practice, for the  
 301 problem considered in section 3, they will be set to 400km and 5 days in space and time,  
 302 ensuring enough observations to resolve the total current at this space/time scale.

303 The  $p^{\text{th}}$  column of  $\mathbf{G}_2$  matrix involved in the inversion is shown on the right panel  
 304 of Figure 4 for illustration. It represents the projection of the sub-component vector field  
 305 at the location and azimuth angle of all observations in the local domain.

### 306 2.3.2.3 Low-frequency ageostrophy: divergent part

307 The divergent part is handled exactly the same way as the rotational part, except  
 308 that the gridded field to resolve is a Solenoidal function  $\mathbf{S}$ , such as the gridded SSH and  
 309 currents  $(\mathbf{H}_3, \mathbf{U}_3, \mathbf{V}_3)$  for this component are written

$$\begin{cases} H_3 = 0 \\ U_3 = -\frac{\partial S}{\partial x} \\ V_3 = -\frac{\partial S}{\partial y} \end{cases} \quad (24)$$

310 Here again, we consider no contributions of  $\mathbf{S}$  on SSH. Following the same reduced-state  
 311 decomposition for  $\mathbf{S}$  than for  $\mathbf{P}$ , with a matrix noted  $\mathbf{\Gamma}_{3_S}$ , the matrices  $\mathbf{\Gamma}_{3_h}$ ,  $\mathbf{\Gamma}_{3_u}$  and  
 312  $\mathbf{\Gamma}_{3_v}$  writes

$$\begin{cases} \Gamma_{3,h}[i, p] = 0 \\ \Gamma_{3,u}[i, p] = -\frac{\partial \Gamma_{3,S}[i, p]}{\partial x_i} \\ \Gamma_{3,v}[i, p] = -\frac{\partial \Gamma_{3,S}[i, p]}{\partial y_i} \end{cases} \quad (25)$$

313 The  $p^{\text{th}}$  column of  $(\mathbf{\Gamma}_{3_u}, \mathbf{\Gamma}_{3_v})$  is represented on the left panel of Figure 5 for illustra-  
 314 tion, as well as the  $p^{\text{th}}$  column of the  $\mathbf{G}_2$  matrix involved in the inversion.

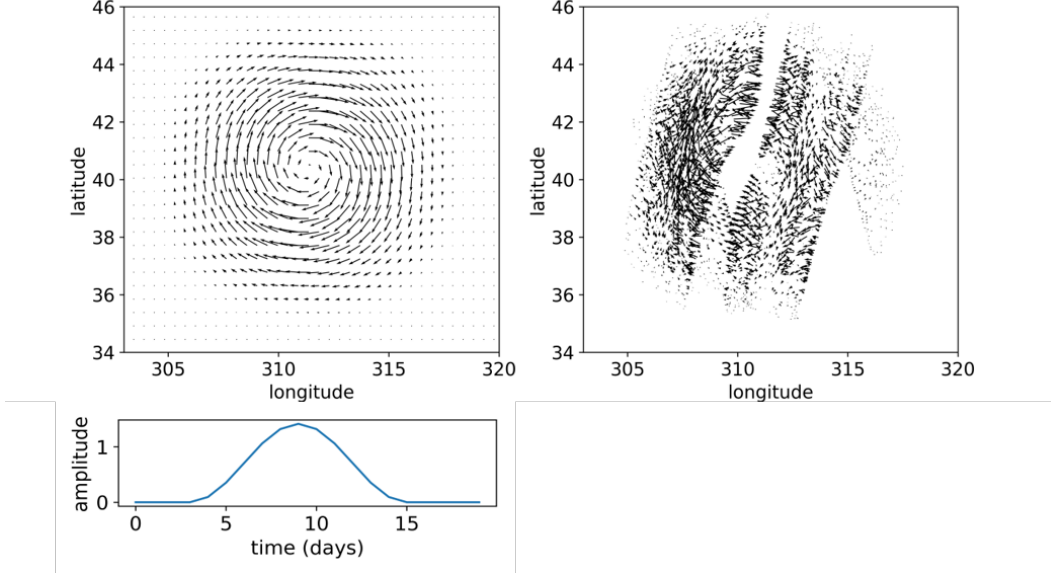


Figure 4: Illustration of a sub-component belonging to the low-frequency ageostrophic rotational component. The upper-left panel represents its expression in the grid space (= a column of the  $\mathbf{\Gamma}_2$  matrix), the arrows for ( $\mathbf{\Gamma}_{2,u}$  and  $\mathbf{\Gamma}_{2,v}$ ), as a function of space. The lower-left panel represent the temporal modulation. The right panel represents the same sub-component in observation space, noted  $\mathbf{G}_{2,u,r}$ .

#### 2.3.2.4 High-frequency ageostrophy (NIO)

This component stands for the near inertial motions featuring very distinct oscillating patterns near the inertia frequency  $f_c$ . It is possible to define a reduced space made of two gridded fields to resolve  $\mathbf{A}$  and  $\mathbf{B}$ , slowly varying in time and space with the gridded SSH and current field ( $H_4, U_4, V_4$ ) expressed as follows

$$\begin{cases} H_4 = 0 \\ U_4 = A \cos(-2\pi f_c t) + B \sin(-2\pi f_c t) \\ V_4 = A \sin(-2\pi f_c t) - B \cos(-2\pi f_c t) \end{cases} \quad (26)$$

Here again, we assume no contribution on SSH. This current field oscillates near the inertia frequency, with a coherency related to the time variations of  $\mathbf{A}$  and  $\mathbf{B}$ . Note that the distinct  $\mathbf{A}$  and  $\mathbf{B}$  allow the degree of freedom on the phase of the NIOs. The reduced space for  $\mathbf{A}$  and  $\mathbf{B}$  is defined by the following  $\mathbf{\Gamma}_{4,A}$  and  $\mathbf{\Gamma}_{4,B}$  identical matrices, giving

$$\Gamma_{4,A}[i, p] = \Gamma_{4,B}[i, p] = e^{-\frac{|t_i - t_p|^q}{\tau^q}} f_{\text{tap}}\left(\frac{x_i - x_p}{L_x}, \frac{y_i - y_p}{L_y}, 0\right) \quad (27)$$

We note that the time decay is not set with the  $f_{\text{tap}}$  function, but with an exponential of degree  $q$  which seemed to better represent actual time perturbations of the oscillations. For the problem considered in section 3,  $L_x$  and  $L_y$  will be both set to 250km,  $q$  at 2 and  $\tau$  at 3 days. These values were optimized to fit the covariance properties of the NIOs signal in the reference simulation. Using eq. (26), the matrices  $\mathbf{\Gamma}_{4,h}$ ,  $\mathbf{\Gamma}_{4,u}$  and  $\mathbf{\Gamma}_{4,v}$  writes

$$\begin{cases} \Gamma_{4,h}[i, p] = 0 \\ \Gamma_{4,u}[i, p] = \Gamma_{4,A}[i, p] \cos(-2\pi f_c t) + \Gamma_{4,B}[i, p] \sin(-2\pi f_c t) \\ \Gamma_{4,v}[i, p] = \Gamma_{4,A}[i, p] \sin(-2\pi f_c t) - \Gamma_{4,B}[i, p] \cos(-2\pi f_c t) \end{cases} \quad (28)$$

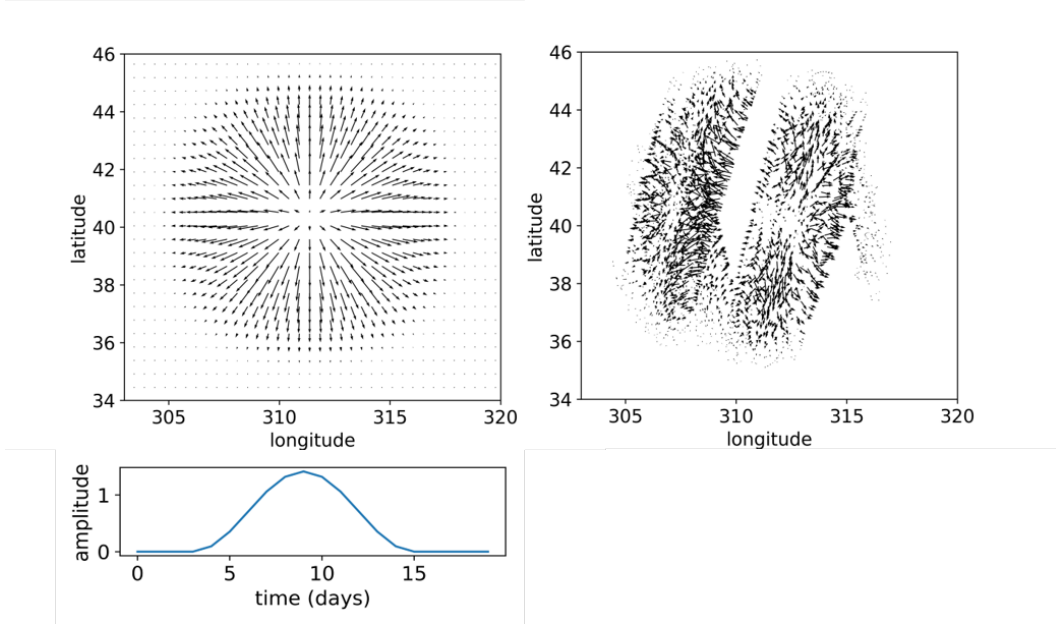


Figure 5: Illustration of a sub-component belonging to the low-frequency ageostrophic divergent component. The upper-left panel represents its expression in the grid space (= a column of the  $\mathbf{\Gamma}_3$  matrix), the arrows for  $(\mathbf{\Gamma}_{3_u}$  and  $\mathbf{\Gamma}_{3_v})$ , as a function of space. The lower-left panel represent the temporal modulation. The right panel represents the same sub-component in observation space, noted  $\mathbf{G}_{3_{ur}}$ .

329 The  $p^{\text{th}}$  column of  $(\mathbf{\Gamma}_{4_u}, \mathbf{\Gamma}_{4_v})$  is represented on the left panels of Figure 6 for illustration.  
 330 The arrows on the upper panel indicate a spatially coherent pattern of NIOs, ac-  
 331 tually rotating in time as indicated by the time-modulation on the lower panel.

332 Finally, the  $p^{\text{th}}$  column of the  $\mathbf{G}_4$  matrix involved in the inversion is shown on the  
 333 right panel of Figure 6. The arrows indicate multiple directions are the observations span  
 334 over different times in the local domain of the sub-component.

### 335 3 Observing System Simulation Experiments

#### 336 3.1 The reference scene

337 Ocean circulation numerical models provide realistic scenes of ocean variability, use-  
 338 ful to assess the impact of existing and future observing systems.

339 In this study, we used the outputs of a high-resolution ( $1/60^\circ$  in the horizontal) sim-  
 340 ulation at hourly frequency, the NEMO NATL60-CJM simulation further described in  
 341 (Amores et al., 2018). This simulation, forced with hourly winds, allows the resolution  
 342 of a wide spectrum of processes at ocean surface, from basin to sub-mesoscales and from  
 343 annual to hourly scales including NIOs, in the North Atlantic region. This simulation  
 344 does not include tidal forcing, but as discussed in the conclusion, this should not impact  
 345 our analysis. The SSH and surface current in the first layer constitute our ground-truths  
 346 in the experiments spanning over the year 2012.

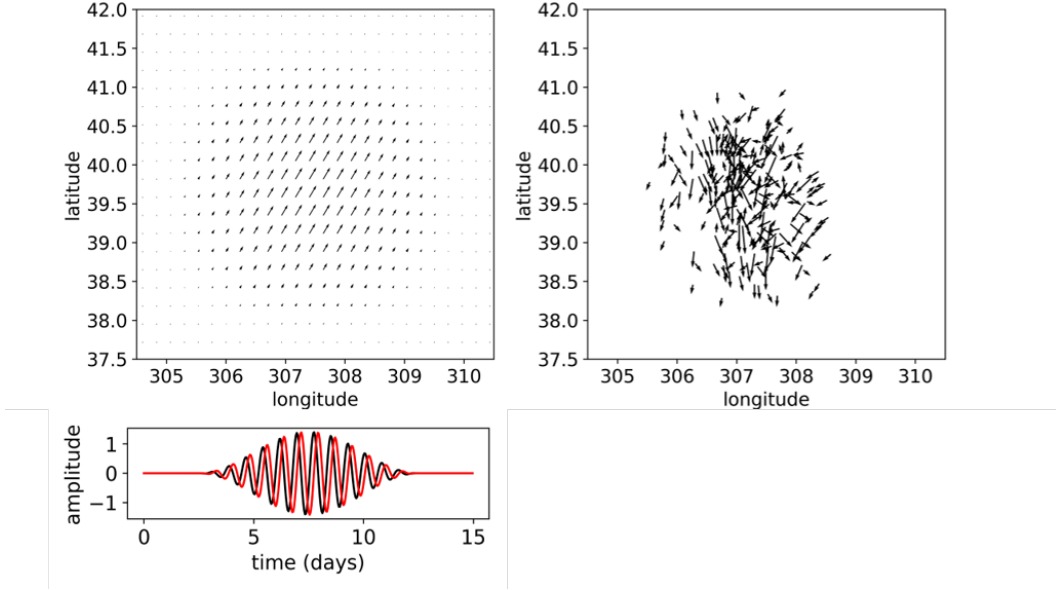


Figure 6: Illustration of a sub-component belonging to the high-frequency ageostrophic component. The upper-left panel represents its expression in the grid space (and corresponds to a column of the  $\Gamma_4$  matrix), the arrows for  $(\Gamma_{4u}$  and  $\Gamma_{4v})$ , as a function of space. The lower-left panel represent the temporal modulation for the zonal u (black) and meridional v (red) components. The right panel represents the same sub-component in observation space, noted  $G_{4u_r}$ .

347

### 3.2 Synthetic observations from instrument simulators

348

The instrument simulators are based on existing software used to generate synthetic observations. They perform a sampling, in time and space, of the reference scene over the satellite view along the orbit, and generate a realistic measurement error, either instrumental or geophysical.

349

350

#### 3.2.1 The altimetry simulator

351

The altimetry simulator (Gaultier et al., 2016) in its nadir version was used in this study to simulate a constellation of 5 altimeters on different orbits (two Jason-like and three Sentinel3-like). The model SSH was sampled at 1 Hz posting (approximately 6 km) along these orbit tracks over 1-year. An instrumental error of 3cm RMS at 1Hz was applied to all satellites following a random Gaussian law to simulate the white-noise plateau. An illustration of the altimetry dataset is shown on the top panels of Figure 7.

352

353

#### 3.2.2 The Doppler simulator

354

The Doppler simulator for the SKIM concept, called 'SKIMulator' (Gaultier, 2019a, 2019b), was developed in the context of SKIM phase A studies by ESA (ESA, 2019). The simulator was applied on the first-layer vector current of the reference field, providing radial current vectors along multiple azimuth angles of the rotating beams as illustrated by the green arrows on Figure 8. An instrument error is applied, accounting for radar noise and Doppler processing errors such as the error in the surface wave Doppler retrieval, as further described in (F. Ardhuin et al., 2019). The total error is on the order of 5-10

355

356

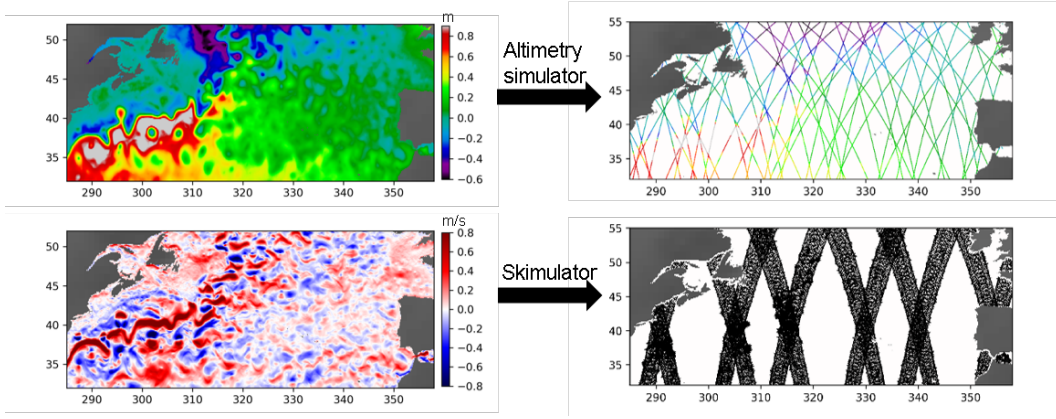


Figure 7: Schematic showing the instrument simulator sampling (altimetry on the top, doppler current Skimulator on the bottom) from the reference scene on the left to the sampled data with instrument error added on the right. Three-day worth of synthetic data are shown on the right panels.

367 cm/s. The overall swath, of 270km width, samples any given point of the Ocean at orbit repeat (12days), and according to the latitude, the ascending/descending and overlapping swaths allow several revisits at different intervals.

## 370 4 Results

### 371 4.1 Reconstruction of Geostrophic and Ageostrophic current

372 The reconstructed geostrophic current (zonal and meridional) compares well with the reference (geostrophic component derived from the reference *SSH*) as suggested by 373 Figure 9 for both basic and improved mapping. Minor differences appear with slightly 374 finer structures in the second case with error fields slightly reduced (3rd versus 5th rows 375 on the figure). This will be quantified in section 4.2 376

377 The left three panels of figure 10 shows the same snapshots (reference, basic and improved mapping) for the ageostrophic component. The reference ageostrophic field on 378 the top is the reference total current minus the reference geostrophic current. Here, as 379 opposed to geostrophy, the fields are fairly different. The temporal evolution of these fields 380 is shown for a selected location on the right panel. First, we note the reference current 381 is composed of periodic fluctuations of approximate near-inertial frequency on top of a 382 slower signal. The spatial scales of the dominant patterns is larger than the mesoscale 383 eddies, probably linked to the atmospheric wind patterns. Estimated ageostrophic 384 field with basic mapping clearly fails on several aspects. By construction, inertial motions 385 are not resolved since they occur at a much higher frequency than the filtering scales 386 of the basic mapping so the time series (blue line) does not feature oscillations. Further- 387 more, the low frequency component does not seem accurate. Given the small number 388 of Doppler instrument revisits (as represented by the grey diamonds on the right panel) 389 the estimation suffers from aliasing. For instance, between days 15 and 30, the obser- 390 vations happen to occur primarily near the maxima of the oscillations for the zonal 391 component, leading to overestimation of the zonal component at low-frequency (blue curve) 392 in this particular case. However, the estimated ageostrophic field with improved map- 393 ping is fairly different. It does resolve inertial motions, and succeeds in capturing, to a 394 large extent, their modulation and phase. The reconstruction capability is based on the 395 degrees of freedom of the signal with respect to the number of independent observations. 396

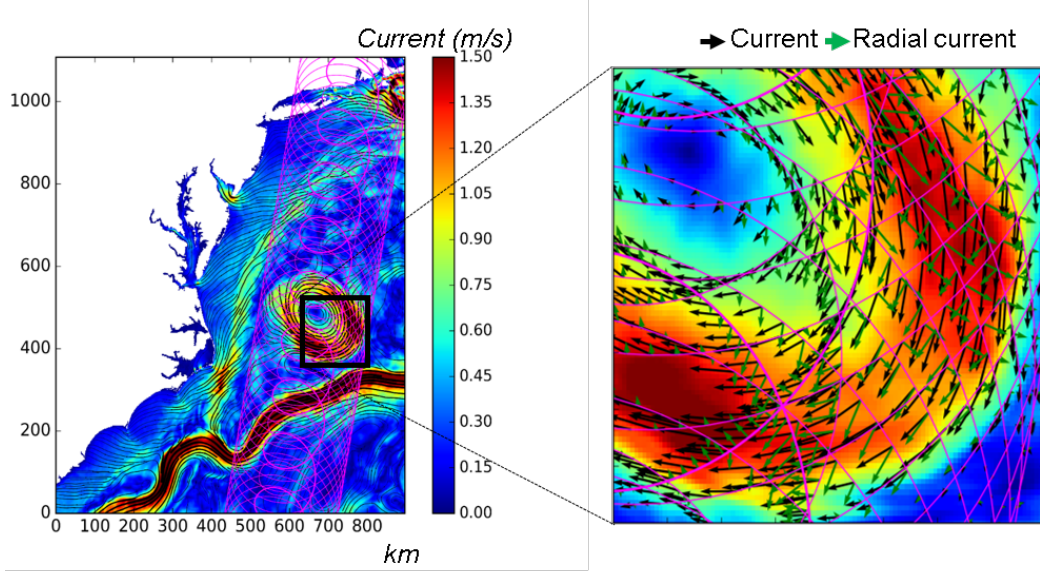


Figure 8: Detailed view of the SKIMulator outputs showing, with respect to the reference 2D current vectors in black, the observed radial current along the satellite azimuth angles in green.

397 Since the spatial patterns of our "true" NIOs are quite large and their temporal exten-  
 398 sion exceeds a few inertial periods, a large volume in time/space can be constrained with  
 399 the Doppler observations. From the reconstructed series (red line on the right panel),  
 400 it is also clear that the low frequency variations of the ageostrophy current is better re-  
 401 solved, the aliasing issue being now mitigated.

402 We illustrate on Figure 11 the total current(represented by local Lagrangian tra-  
 403 jectories) obtained with the two methods. The effect of resolving inertial motions clearly  
 404 shows up on the Lagrangian trajectories, looping like actual drifter trajectories when the  
 405 near inertial current amplitudes exceeds the low-frequency current.

#### 406 4.2 Reconstruction skills as a function of spatial and temporal scales

407 We propose a quantitative analysis of the reconstructions, both in the spatial and  
 408 temporal spectral domain. This will validate the results discussed above and further shed  
 409 light on the reconstruction skills as a function of spatio-temporal scales. The analysis  
 410 is based on the spectral ratio of the error over the true signal, computed along spatial  
 411 or temporal sections of the domain. For spatial analysis, the computation is similar to  
 412 what was proposed in (Ballarotta et al., 2019) to assess the effective resolution of Sea  
 413 Level Anomaly products, but on the velocity in the normal direction of the section. For  
 414 temporal analysis, the rotary spectra are considered for the spectral ratio, leading to two  
 415 separate estimates in the clockwise and counter-clockwise directions. These ratios  $r$   
 416 are represented under the form of a percent scores  $100*(1-r)$  summarized on Figures 12  
 417 and 13 for the different runs and components. As suggested by the upper panels of Fig-  
 418 ure 12, for geostrophic reconstructions, the improvements from basic mapping (green curves)  
 419 to improved mapping (red curves) are sensible at all scales, especially below 150km. If  
 420 we consider 50% as a reasonable threshold, then the resolving capabilities of the altime-  
 421 ter reconstruction for zonal and meridional current is about 110km, and 90km with SKIM  
 422 combination. This is still a fair improvement for a single instrument added to an exist-  
 423 ing 5-instrument constellation. From this experiment, the Doppler observations would

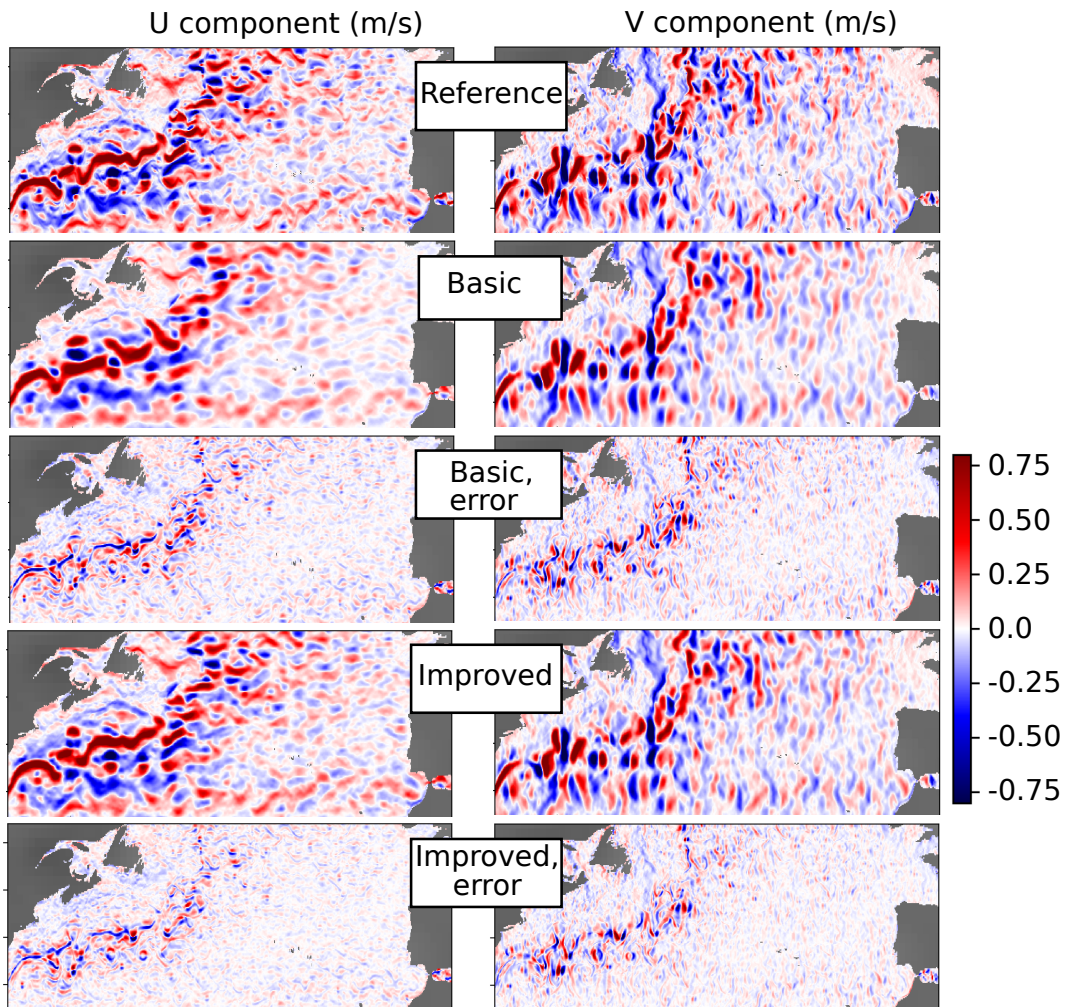


Figure 9: Snapshots of the geostrophic component (m/s) in the zonal (left column) and meridional (right column) directions, with differences (errors). The upper row is the reference, the second and third rows are the basic reconstructions and errors (w.r.t. reference) respectively. The fourth and fifth rows are the same as second and third for the improved mapping.

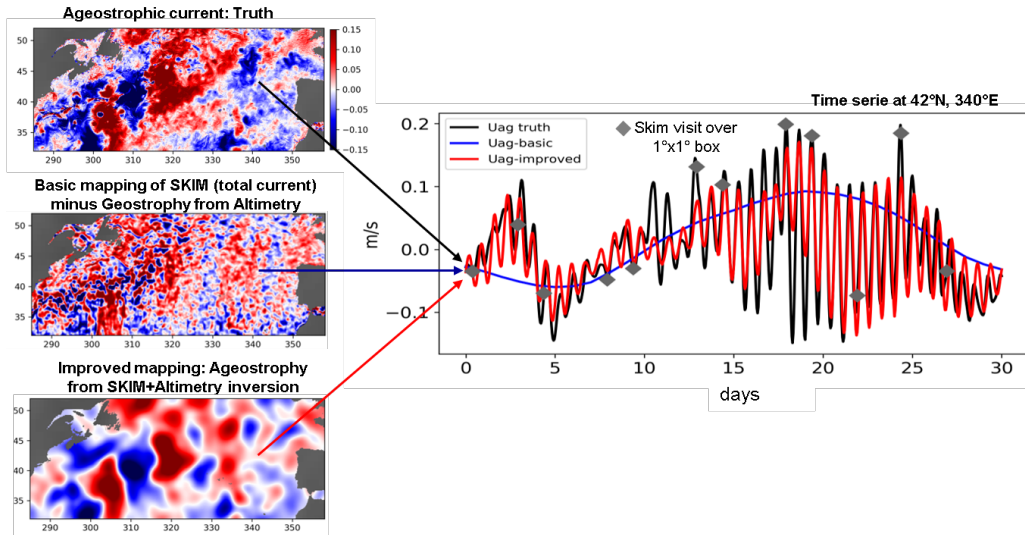


Figure 10: Reconstruction of the zonal ageostrophic component compared to the reference, in m/s. Upper left panel: snapshot of true (reference) ageostrophic zonal current. Middle left panel: reconstruction from basic mapping. Lower left panel: reconstruction from improved mapping. Right panel: time series of the reference (black), basic mapping (blue) and improved mapping (red) at  $340^{\circ}\text{E}$ ,  $42^{\circ}\text{N}$  as a function of time over a month.

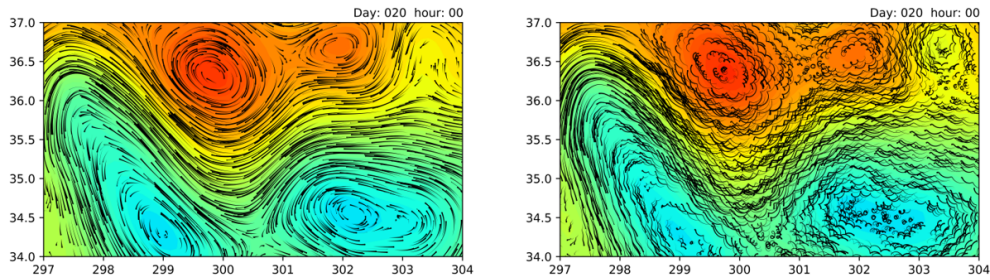


Figure 11: SSH (plain color) and local Lagrangian trajectories (black lines) of the surface current resolved with basic (left) and improved (right) mapping.

424 therefore improve the geostrophic component reconstruction even though altimetry is  
 425 already efficient to capture this particular component. An additional experiment was led  
 426 with improved mapping from Doppler observations only, represented in blue on the fig-  
 427 ure. The performances are not as good as with the combination, but do exceed those of  
 428 altimetry only at small scales (below 250km). At large scales, the ambiguity with ageostro-  
 429 phy, in absence of altimetry, certainly explains the lower performances.

430 We also note minor differences between the zonal and meridional performances: at  
 431 large scales beyond 250km, the meridional component seems slightly better resolved with  
 432 altimetry and SKIM, meaning that the zonal gradients of SSH would be more accurate  
 433 at these large scales. With SKIM, the design was indeed found to perform better for along-

434 track azimuth angles on swath average (Gaultier, 2019b) resulting in slightly better meridional  
 435 currents on global average.

436 For ageostrophic reconstructions (lower panels of Figure 12), more sensitive differ-  
 437 ences were found as expected. Indeed, with the basic mapping, only the largest scales  
 438 are partially resolved. Because of aliasing issues discussed in 4.1, the portion of resolved  
 439 signal is weak, of about 15% (zonal) to 30% (meridional) beyond 1000km wavelength.  
 440 However, the reconstruction with improved mapping exceeds 45% above 500km, where  
 441 most of the inertial energy is. Note that, by construction of the sub-components for ageostrophic  
 442 current, we do not aim to resolve scales below 300km. This could be explored, but do-  
 443 ing so with this observing system would be a challenge because of high-temporal frequen-  
 444 cies at short spatial scales. The dashed lines, showing the NIO contribution only, indeed  
 445 suggest that most of the improvements owe to the inertial part. The experiment with  
 446 Doppler observations only (blue curve) also brings interesting results. The drop in per-  
 447 formances, especially at large scales, suggests the importance of an altimetry constella-  
 448 tion the better separate the geostrophic contribution and therefore better estimate the  
 449 ageostrophic component as well.

450 The score evaluations in the time-frequency domain (Figure 13) bring additional  
 451 elements, in particular about the low-frequency ageostrophy, by comparing the plain (NIO+  
 452 low-frequency ageostrophy) with the dashed (NIO only) lines on the lower panels. The  
 453 low-frequency ageostrophy is indeed an essential component, allowing a reconstruction  
 454 score above 50% to 60% beyond a week period. We also found (not shown) that the ro-  
 455 tational part was dominant over the divergent part, which is not surprising since the low  
 456 frequency wind should be directly related to low-frequency wind, mostly rotational. The  
 457 inertial peak appears also clearly on the scores at around 16 hours in the clockwise di-  
 458 rection (lower-left panel). For geostrophy (upper panels) the time window does not al-  
 459 low to fully resolve the eddy time band (mostly beyond a month) where scores would  
 460 reach the values found in the spatial analysis. However, the relative scores are consis-  
 461 tent, we note that the relative improvement between the two methods (green versus red)  
 462 are high between 5 and 10 days, suggesting that the time aliasing mitigation is efficient.  
 463 We also note no significant differences between clockwise and counter-clockwise direc-  
 464 tions, as expected since quasi-geostrophic motions have similar energy for the two com-  
 465 ponents of their rotary spectra.

## 466 5 Conclusions and perspectives

467 This study demonstrated, in principle, the possibility to disentangle and map vari-  
 468 ous components of the ocean surface current from partial observations of the surface dy-  
 469 namic topography and current. This was achieved thanks to a specific treatment of the  
 470 covariance structures used in the mapping. Indeed, for mid-latitudes the time revisits  
 471 of proposed spaceborne instruments for surface current measurements exceeded half the  
 472 inertial periods, where a large part of the signal energy is. Basic mapping algorithms,  
 473 acting as a low-pass filter, not surprisingly fail in resolving those signals and also intro-  
 474 duce strong aliasing. The improved mapping presented here performs well thanks to the  
 475 spatial and temporal coherence of high-frequency signals, long enough with respect to  
 476 observation sampling. However, several additional tests (not shown) also show that in-  
 477 creasing the time sampling, with a wider swath such as proposed in the WaCM or STREAM  
 478 design, or a constellation of several SKIM-like satellites can resolve a much larger frac-  
 479 tion of the NIOs variance even if it comes with higher instrumental noise. The present  
 480 work therefore should help in the identification of trade-offs for the optimization of Doppler  
 481 scatterometer designs and orbit choice. In general altimetry is an essential source of ob-  
 482 servations in addition to Doppler scatterometers, in particular to disentangle the sur-  
 483 face current components.

484 The results of the reconstruction method considered in this study probably depends  
 485 on the basis of sub-components chosen. This latter have been constructed manually with

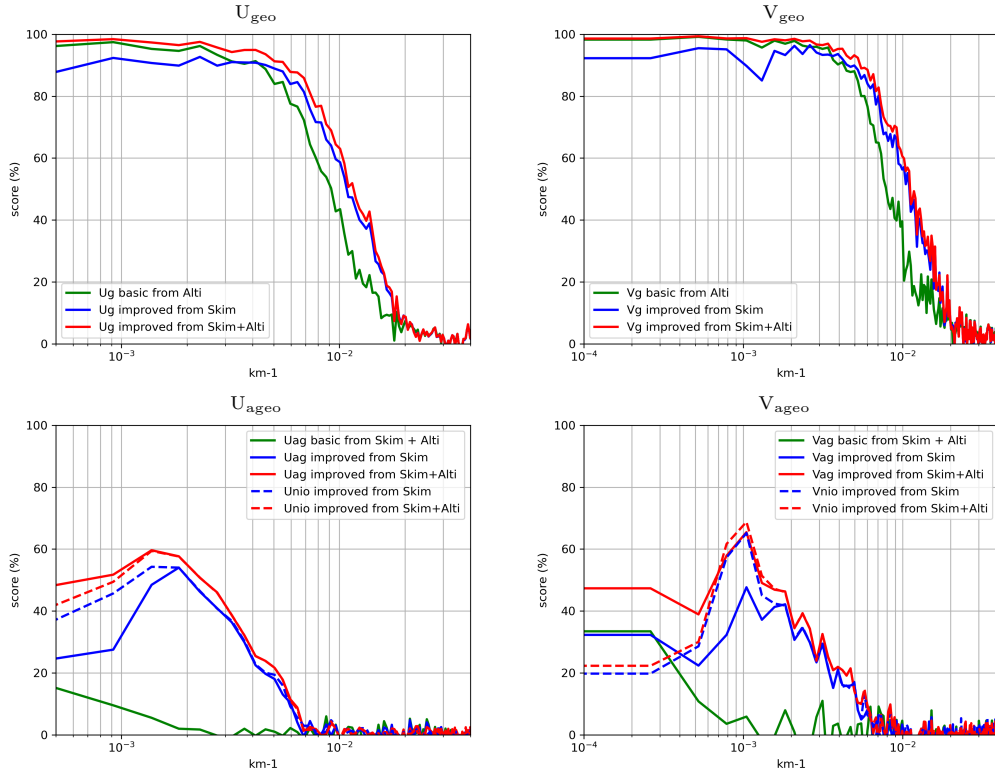


Figure 12: Performances as a function of spatial wavelength computed, in percent, from the ratio of the reconstruction error spectrum by the true signal spectrum. 100% means a full reconstruction with no errors. Upper-left panel: Scores for geostrophic zonal current with basic mapping of altimetry (green), with improved mapping of SKIM (blue) and with improved mapping of SKIM + Altimetry combined (red). Upper-right panel: same for meridional current. Lower-left panel: scores for ageostrophic zonal current with basic mapping of SKIM + Altimetry combined (green), with improved mapping of SKIM (blue) and with improved mapping of SKIM + Altimetry combined (red). The dashed lines represent the contribution of near-inertial current only. Lower-right panel: same for meridional current.

486 a wavelet basis approach, accounting for coherent structures seen in the different component  
 487 of the flow considered. This method has the limitation to project observations  
 488 on prescribed bases, requiring a priori knowledge of the signal characteristics ( $\mathbf{G}$  matrix)  
 489 and statistics ( $\mathbf{Q}$  matrix). Also, potential interactions between the components, for instance  
 490 the impact of mesoscale eddies on inertial oscillations through relative vorticity  
 491 fluctuations, is not yet accounted. We also acknowledge that tidal currents have not been  
 492 considered in this experiment as the reference run is tide-free. However, dedicated analyses  
 493 presented in (F. e. a. Arduin, 2019) suggest that tidal current may be well handled thanks  
 494 to accurate barotropic models and favorable orbit aliasing. Baroclinic tidal currents, not  
 495 always phase locked (Zaron, 2019) may also be a challenge, but they probably are dominated  
 496 by shorter scales with a minimal interaction with inertial oscillation.

497 The practical applicability of the present result strongly depends on the realism  
 498 of the surface current field, in particular its ageostrophic component. A preliminary analysis  
 499 of drifter pairs, which will be reported elsewhere, suggests that half of the velocity  
 500 variance is contained in covariances with scales larger than 100 km (Xiaolong Yu, personal  
 501 communication 2019). We thus expect that the present approach is qualitatively

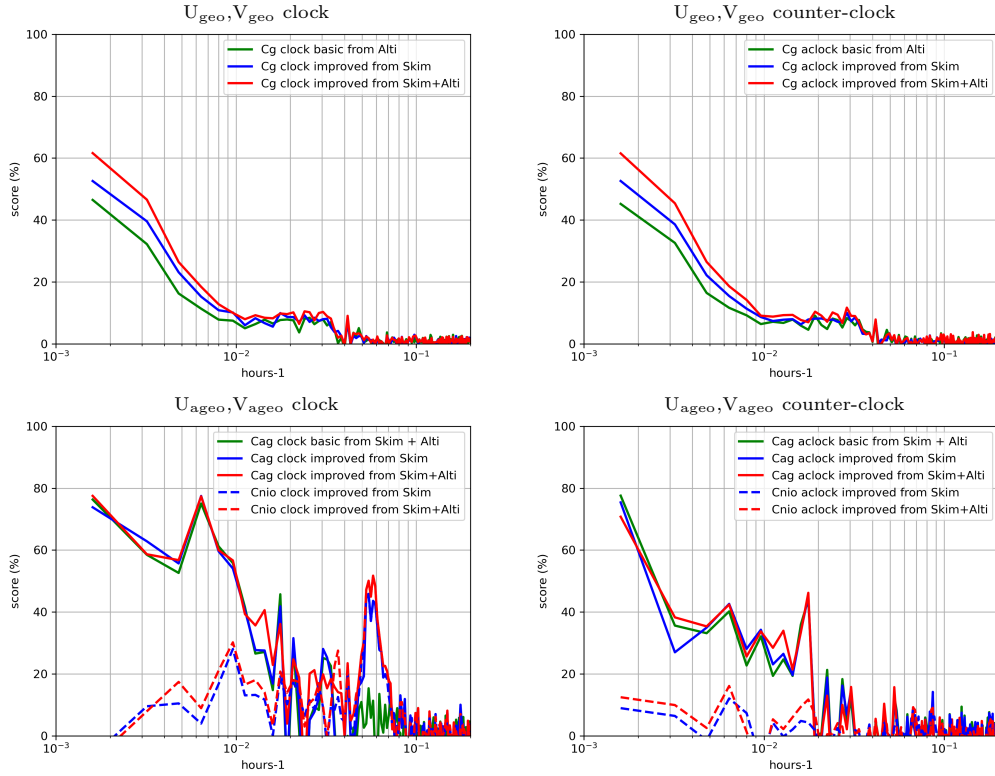


Figure 13: Performances as a function of temporal frequency computed, in percent, from the ratio of the reconstruction error rotary spectrum by the true signal error rotary spectrum. Upper-left panel: Scores for geostrophic clockwise current with basic mapping of Altimetry (green), with improved mapping of SKIM (blue) and with improved mapping of SKIM + Altimetry combined (red). Upper-right panel: same for counter-clockwise current. Lower-left panel: scores for ageostrophic clockwise current with basic mapping of SKIM + Altimetry combined (green), with improved mapping of SKIM (blue) and with improved mapping of SKIM + Altimetry combined (red). The dashed lines represent the contribution of near-inertial current only. Lower-right panel: same for counter-clockwise current.

502 valid, and that there may also be a chance to successfully invert some near inertial cur-  
 503 rent from the drifters alone in regions of high drifter density like subtropical Gyres.

504 **Acknowledgments**

505 This study was funded by the Centre National d’Etudes Spatiales (CNES) as part as  
 506 the SKIM phase A contract for the mapping algorithm developed in section 2.3 and by  
 507 the European Space Agency (ESA) as part of the SKIM-SciSoc contract for the map-  
 508 ping algorithm implemented in section 2.2.

509 All data used in this study (reference fields, synthetic observations and gridded anal-  
 510 ysis) are available on the following repository: [ongoing, see ‘materials for reviewers’]

511 **References**

512 Amores, A., Jordà, G., Arsouze, T., & Le Sommer, J. (2018). Up to what ex-  
 513 tent can we characterize ocean eddies using present-day gridded altimetric

- 514 products? *Journal of Geophysical Research: Oceans*, 123(10), 7220-7236.  
 515 Retrieved from [https://agupubs.onlinelibrary.wiley.com/doi/abs/](https://agupubs.onlinelibrary.wiley.com/doi/abs/10.1029/2018JC014140)  
 516 10.1029/2018JC014140 doi: 10.1029/2018JC014140
- 517 Ardhuin, Brandt, P., Gaultier, L., Donlon, C., Battaglia, A., Boy, F., ... Stam-  
 518 mer, D. (2019). Skim, a candidate satellite mission exploring global ocean  
 519 currents and waves. *Frontiers in Marine Science*, 6, 209. Retrieved from  
 520 <https://www.frontiersin.org/article/10.3389/fmars.2019.00209> doi:  
 521 10.3389/fmars.2019.00209
- 522 Ardhuin, Chapron, B., Maes, C., Romeiser, R., Gommenginger, C., Cravatte, S., ...  
 523 Bourassa, M. (2019). Satellite doppler observations for the motions of the  
 524 oceans. , 100. doi: 10.1175/BAMS-D-19-0039.1
- 525 Ardhuin, F., Chapron, B., Marié, L., Gressani, V., Nouguier, F., Delouis, J.-M.,  
 526 & Peureux, C. (2019, 05). *Estimation of non-geophysical doppler and wave*  
 527 *doppler, and inversion algorithm for skim*. doi: 10.13140/RG.2.2.22907.98081/  
 528 3
- 529 Ardhuin, F. e. a. (2019, 05). *Earth explorer 9 candidate mission skim –report for*  
 530 *mission selection*.
- 531 Ballarotta, M., Ubelmann, C., Pujol, M.-I., Taburet, G., Fournier, F., Leg-  
 532 eais, J.-F., ... Picot, N. (2019). On the resolutions of ocean altimetry  
 533 maps. *Ocean Science Discussions*, 2019, 1–27. Retrieved from [https://](https://www.ocean-sci-discuss.net/os-2018-156/)  
 534 [www.ocean-sci-discuss.net/os-2018-156/](https://www.ocean-sci-discuss.net/os-2018-156/) doi: 10.5194/os-2018-156
- 535 Carrère, L., & Lyard, F. (2003). Modeling the barotropic response of the global  
 536 ocean to atmospheric wind and pressure forcing - comparisons with obser-  
 537 vations. *Geophysical Research Letters*, 30(6). Retrieved from [https://](https://agupubs.onlinelibrary.wiley.com/doi/abs/10.1029/2002GL016473)  
 538 [agupubs.onlinelibrary.wiley.com/doi/abs/10.1029/2002GL016473](https://agupubs.onlinelibrary.wiley.com/doi/abs/10.1029/2002GL016473) doi:  
 539 10.1029/2002GL016473
- 540 D'Asaro, E. A. (1985). The energy flux from the wind to near-inertial motions in the  
 541 surface mixed layer. *Journal of Physical Oceanography*, 15(8), 1043-1059. Re-  
 542 trieved from [https://doi.org/10.1175/1520-0485\(1985\)015<1043:TEFFTW>](https://doi.org/10.1175/1520-0485(1985)015<1043:TEFFTW>2.0.CO;2)  
 543 2.0.CO;2 doi: 10.1175/1520-0485(1985)015<1043:TEFFTW>2.0.CO;2
- 544 Elipot, S., Lumpkin, R., Perez, R. C., Lilly, J. M., Early, J. J., & Sykulski, A. M.  
 545 (2016). A global surface drifter data set at hourly resolution. *Jour-*  
 546 *nal of Geophysical Research: Oceans*, 121(5), 2937–2966. Retrieved from  
 547 <http://dx.doi.org/10.1002/2016JC011716> doi: 10.1002/2016JC011716
- 548 Elipot, S., Lumpkin, R., & Prieto, G. (2010). Modification of inertial oscillations by  
 549 the mesoscale eddy field. *Journal of Geophysical Research: Oceans*, 115(C9).  
 550 Retrieved from [https://agupubs.onlinelibrary.wiley.com/doi/abs/](https://agupubs.onlinelibrary.wiley.com/doi/abs/10.1029/2009JC005679)  
 551 10.1029/2009JC005679 doi: 10.1029/2009JC005679
- 552 ESA. (2019, May). *Report for mission selection: SKIM* (Tech. Rep. No. ESA-  
 553 EOPSM-SKIM-RP-3550). European Space Agency, Noordwijk, The Nether-  
 554 lands. doi: 10.13140/RG.2.2.22907.98081/3
- 555 Fu, L.-L., Chelton, D. B., & Zlotnicki, V. (1988, November). Satellite altimetry:  
 556 Observing ocean variability from space. *Oceanography*, 1. Retrieved from  
 557 <https://doi.org/10.5670/oceanog.1988.01>
- 558 Gaultier, L. (2019a). *Skimulator repository*. [https://github.com/oceandatalab/](https://github.com/oceandatalab/skimulator)  
 559 [skimulator](https://github.com/oceandatalab/skimulator). GitHub.
- 560 Gaultier, L. (2019b). *Skimulator user manual* [Computer software manual]. Re-  
 561 trieved from [https://github.com/oceandatalab/skimulator/blob/master/](https://github.com/oceandatalab/skimulator/blob/master/doc/source/science.rst)  
 562 [doc/source/science.rst](https://github.com/oceandatalab/skimulator/blob/master/doc/source/science.rst)
- 563 Gaultier, L., Ubelmann, C., & Fu, L.-L. (2016). The challenge of using future swot  
 564 data for oceanic field reconstruction. *Journal of Atmospheric and Oceanic*  
 565 *Technology*, 33(1), 119-126. Retrieved from [https://doi.org/10.1175/](https://doi.org/10.1175/JTECH-D-15-0160.1)  
 566 10.1175/JTECH-D-15-0160.1 doi: 10.1175/JTECH-D-15-0160.1
- 567 Gille, S. T., & Hughes, C. W. (2001). Aliasing of high-frequency variability by  
 568 altimetry: Evaluation from bottom pressure recorders. *Geophysical Research*

- 569 *Letters*, 28(9), 1755-1758. Retrieved from <https://agupubs.onlinelibrary>  
570 [.wiley.com/doi/abs/10.1029/2000GL012244](https://agupubs.onlinelibrary.wiley.com/doi/abs/10.1029/2000GL012244) doi: 10.1029/2000GL012244
- 571 Gommenginger, C., Chapron, B., Hogg, A., Buckingham, C., Fox-Kemper, B., Eriks-  
572 son, L., ... Burbidge, G. (2019). Seastar: A mission to study ocean sub-  
573 mesoscale dynamics and small-scale atmosphere-ocean processes in coastal,  
574 shelf and polar seas. *Frontiers in Marine Science*, 6, 457. Retrieved from  
575 <https://www.frontiersin.org/article/10.3389/fmars.2019.00457> doi:  
576 10.3389/fmars.2019.00457
- 577 Kim, S. Y., Terrill, E. J., & Cornuelle, B. D. (2008). Mapping surface currents from  
578 hf radar radial velocity measurements using optimal interpolation. *Journal of*  
579 *Geophysical Research: Oceans*, 113(C10). Retrieved from <https://agupubs>  
580 [.onlinelibrary.wiley.com/doi/abs/10.1029/2007JC004244](https://agupubs.onlinelibrary.wiley.com/doi/abs/10.1029/2007JC004244) doi: 10.1029/  
581 2007JC004244
- 582 Le Traon, P. Y. L., & Dibarboure, G. (2002). Velocity mapping capabilities of  
583 present and future altimeter missions: The role of high-frequency signals.  
584 *Journal of Atmospheric and Oceanic Technology*, 19(12), 2077-2087. Retrieved  
585 from [https://doi.org/10.1175/1520-0426\(2002\)019<2077:VMCOPA>2.0](https://doi.org/10.1175/1520-0426(2002)019<2077:VMCOPA>2.0)  
586 [.CO;2](https://doi.org/10.1175/1520-0426(2002)019<2077:VMCOPA>2.0.CO;2) doi: 10.1175/1520-0426(2002)019<2077:VMCOPA>2.0.CO;2
- 587 Pollard, R., & Millard, R. (1970). Comparison between observed and simulated  
588 wind-generated inertial oscillations. *Deep Sea Research and Oceanographic*  
589 *Abstracts*, 17(4), 813 - 821. Retrieved from <http://www.sciencedirect.com/>  
590 [science/article/pii/0011747170900434](http://www.sciencedirect.com/science/article/pii/0011747170900434) doi: [https://doi.org/10.1016/](https://doi.org/10.1016/0011-7471(70)90043-4)  
591 [0011-7471\(70\)90043-4](https://doi.org/10.1016/0011-7471(70)90043-4)
- 592 Pujol, M.-I., Faugère, Y., Taburet, G., Dupuy, S., Pelloquin, C., Ablain, M., &  
593 Picot, N. (2016). Duacs dt2014: the new multi-mission altimeter data set  
594 reprocessed over 20 years. *Ocean Science*, 12(5), 1067-1090. Retrieved from  
595 <https://www.ocean-sci.net/12/1067/2016/> doi: 10.5194/os-12-1067-2016
- 596 Rio, M.-H., Mulet, S., & Picot, N. (2014). Beyond goce for the ocean circulation es-  
597 timate: Synergetic use of altimetry, gravimetry, and in situ data provides new  
598 insight into geostrophic and ekman currents. *Geophysical Research Letters*,  
599 41(24), 8918-8925. Retrieved from <https://agupubs.onlinelibrary.wiley>  
600 [.com/doi/abs/10.1002/2014GL061773](https://agupubs.onlinelibrary.wiley.com/doi/abs/10.1002/2014GL061773) doi: 10.1002/2014GL061773
- 601 Rodriguez, E., Wineteer, A., Perkovic-Martin, D., Gál, T., W. Stiles, B., Ni-  
602 amsuwan, N., & Rodriguez Monje, R. (2018, 04). Estimating ocean vector  
603 winds and currents using a ka-band pencil-beam doppler scatterometer. *Re-*  
604 *remote Sensing*, 10, 576. doi: 10.3390/rs10040576
- 605 Rodríguez, E., Bourassa, M., Chelton, D., Farrar, J. T., Long, D., Perkovic-Martin,  
606 D., & Samelson, R. (2019). The winds and currents mission concept. *Frontiers*  
607 *in Marine Science*, 6, 438. Retrieved from <https://www.frontiersin.org/>  
608 [article/10.3389/fmars.2019.00438](https://www.frontiersin.org/article/10.3389/fmars.2019.00438) doi: 10.3389/fmars.2019.00438
- 609 Whitt, D. B., & Thomas, L. N. (2015). Resonant generation and energetics of wind-  
610 forced near-inertial motions in a geostrophic flow. *Journal of Physical Oceanog-*  
611 *raphy*, 45(1), 181-208.
- 612 Young, W., & Jelloul, M. B. (1997). Propagation of near-inertial oscillations through  
613 a geostrophic flow. *Journal of marine research*, 55(4), 735-766.
- 614 Yu, X., Ponte, A. L., Elipot, S., Menemenlis, D., Zaron, E. D., & Abernathey, R.  
615 (2019). Surface kinetic energy distributions in the global oceans from a high-  
616 resolution numerical model and surface drifter observations. *Geophysical*  
617 *Research Letters*, 46, 9757-9766. doi: 10.1029/2019gl083074
- 618 Zaron, E. (2019, 05). Predictability of non-phase-locked baroclinic tides in the  
619 caribbean sea. *Ocean Science Discussions*, 1-23. doi: 10.5194/os-2019-53